New insights in glaciers characterization by differential diagnosis integrating GPR and remote sensing techniques: A case study for the Eastern Gran Zebrù glacier (Central Alps)

E. Forte [a], I. Santin [a,*], S. Ponti [b], R.R. Colucci [c], P. Gutgesell [a], M. Guglielmin [b]

[a] Department of Mathematics and Geosciences, Trieste University, Trieste, Italy
[b] Department of Theoretical and Applied Sciences, Insubria University, Varese, Italy
[c] Institute of Polar Sciences, National Research Council, Venezia, Italy

ARTICLE INFO

ABSTRACT

In GPR profiles, ice is usually imaged as a mostly electromagnetic transparent facies. However, diffraction events, as well as internal layering, can be also observed. In some cases, the bedrock below glaciers is masked by dense diffractions usually interpreted as the effect of liquid water pockets inside the so-called warm ice. However, the actual physical meaning of such GPR facies is not always obvious, because it can be related also to mixed debris and ice deposits.

We adopted a strategy well known in medical sciences and referred as "differential diagnosis" in order to infer which is the actual meaning of a high scattering facies imaged within the Eastern Gran Zebrù glacier (Central Italian Alps) and, more generally, of all the internal glacier features. In fact, in many cases, there is no direct information to limit the subjectivity of geophysical interpretation; therefore, we provide all the discriminative hypotheses based on both independent and integrated criteria including GPR attribute analysis, imaging effects, reflection analysis, GPR frequency evaluations combined with geomorphological and remote sensing data obtained by two photogrammetric UAV and thermal infrared surveys.

On the basis of the differential diagnosis, we concluded that the high scattering zone embedded within the studied glacier is most likely related to a mixture of ice and debris probably formed during a past shrinking phase. Beside this case study, this approach could be helpful in other GPR glaciological surveys, in which the target is related not only to the bedrock detection, but also to a detailed analysis of the internal facies of a glacier.

1. Introduction

Monitoring glaciers' health and their evolution in time can be performed through the combination of several techniques (Karpilo Jr., 2009) spanning from direct measurements, e.g., ice cores (Paterson, 1994) or data of ablation and accumulation rates (Kaser et al., 2003), to indirect analysis, such as geophysical methods and remote sensing techniques (Pellikka and Gareth Rees, 2010; Barzycka et al., 2020) or equilibrium line altitude evolution (e.g. Žebre et al., 2020). The application of unmanned aerial vehicles (UAV) systems and sensors is considered a highly valuable tool to rapidly collect 3D topographic information (Colomina and Molina, 2014; Fugazza et al., 2018) and in glaciology it is increasingly used to investigate different characteristics of glaciers, including mass balance and thermal assessment. Ground-based or air-borne thermal infrared imaging (TIR) can be exploited, among others, to map glaciers surface temperatures (Aubry-Wake et al., 2015), identify surface water infiltration by heat flow measurements (Anderson, 2005) and gain insight on permafrost dynamic in combination with photogrammetric imaging (Van der Sluijs et al., 2018).

Focusing on geophysical methods, and specifically on Ground Penetrating Radar (GPR), it is a non-invasive geophysical technique which aims at high-resolution imaging of the subsurface, exploiting the propagation of high frequency (usually ranging between 10 MHz and 1 GHz) electro-magnetic (EM) waves (Jol, 2009). The propagation of such a signal is mainly affected by the EM properties of the ground, so GPR data can be used to investigate the subsurface structures reaching variable penetration depths. Frozen materials as ice, snow and *firn*, as well as permafrost, are characterized by low overall electrical conductivity,

---
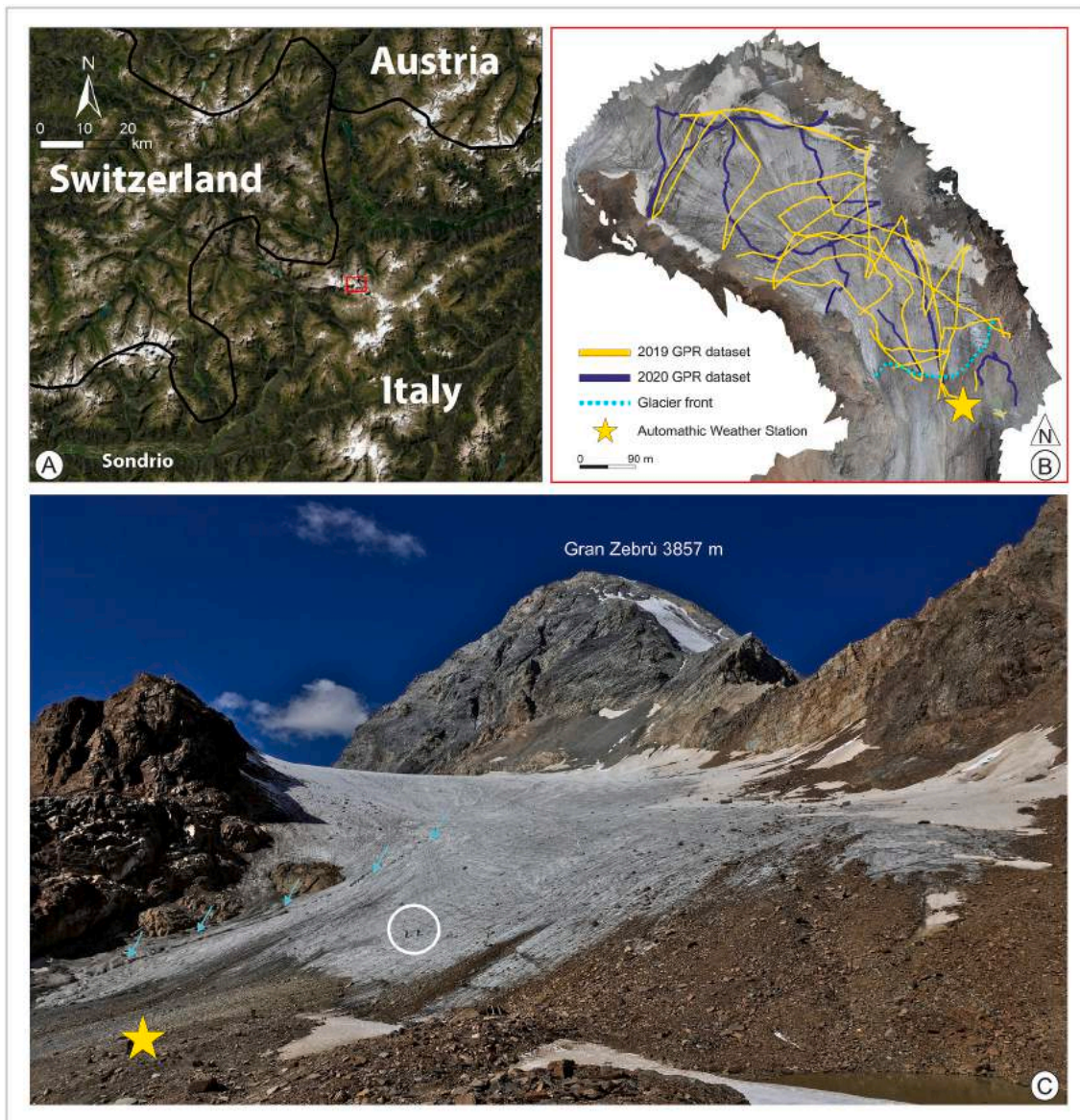
Fig. 1. (A) Location map of the Eastern Gran Zebrù Glacier (EGZ); (B) 2020 Orthophoto of EGZ with superimposed the 2019 (yellow) and 2020 (blue) GPR datasets; (C) Photo of EGZ taken in September 2019, the light-blue arrows mark the bedière flowing down the glacier surface and the white circle highlights two operators during the geophysical survey. Yellow star indicates the position of the Automatic Weather Station. (For interpretation of the references to colour in this figure legend, the reader is referred to the web version of this article.)

usually resulting in very low attenuation of the EM signal, when compared to most of the other geological materials. Therefore, high penetration depths of even hundreds of meters in favourable conditions can be reached and GPR is probably the most exploited geophysical method for glaciological studies. At present, most surveys are performed dragging manually the GPR system on the glacier surface. However, surveys performed with a GPR system mounted on the aerial platforms proved to be a rapid solution for glacier monitoring (Rutishauser et al., 2016), allowing to survey large areas and safely operate in challenging zones (Li et al., 2013; Santin et al., 2019; Catapano et al., 2021). In glaciology, GPR is widely applied to investigate different topics, including the internal imaging of ice bodies (Del Longo et al., 2001; Merz et al., 2014; Colucci et al., 2015) and mass balance estimation through time (Del Gobbo et al., 2016; Santin et al., 2019). GPR is also exploited for glaciers volumes reconstruction (Navarro et al., 2014; Dossi et al., 2018), glaciers hydrology (Moorman and Michel, 2000; Church et al., 2019), snow cover (Godio, 2008; Booth et al., 2013) and ice caves characterization (Hausmann and Behm, 2011; Colucci et al.,

2016) as well as permafrost mapping end monitoring (Campbell et al., 2018).

In a GPR profile, ice is usually displayed by a mostly EM transparent facies, while snow and *firn* can be often recognised by a layering due to seasonal and multi-annual accumulation. However, inside the transparent facies, scattering events can be observed. In case of multiple aligned scattering phenomena, such features are associated to crevasses or shearing zones (Thompson et al., 2020), while distributed diffraction hyperbolas can be indicative of debris inside the ice. Scattering is removed during data processing by applying migration algorithms which focus the EM scattered energy into (or close to) the object which originated the diffraction (e.g. Jol, 2009). However, the actual physical meaning of a highly diffuse scattered facies imaged by GPR is not always obvious. In glaciological studies it is often related to the presence of different quantities of liquid water due to the temperature of the ice, referred as *warm ice* in polythermal glaciers (e.g. Bælum and Benn, 2011). In fact, in polythermal glaciers, there is typically a clear transition from cold to warm ice due to the abrupt change in water content, in

turn related to different thermal regimes (Pettersson et al., 2003). In GPR datasets, this transition is often apparent between an upper level with only few reflections and diffractions and a less transparent zone characterized by diffuse scattering, typically referred to small scale free water filled areas within warm ice (Gacitùa et al., 2015; King et al., 2008; Reinardy et al., 2019). Nevertheless, it is possible that the scattering facies is indicative also for deposits of mixed debris and ice (King et al., 2008; Colucci et al., 2015). So far, both free water and internal debris in fact can produce scattering phenomena, both potentially resulting in the limitation of the investigation depth and in masking the reflection of the ice-bedrock interface (Forte et al., 2015). The distribution of warm and cold ice results in complex and still not fully understood thermal regime, which affects glaciers' hydrology and drainage system (Irvine-Fynn et al., 2011) and is responsible for surging events (Fowler et al., 2001). Thermal characterization of glaciers is a highly investigated issue, especially in Swiss Alps (Eisen et al., 2009; Rutishauser et al., 2016), Scandinavia (Pettersson et al., 2003; Gusmeroli et al., 2012; Reinardy et al., 2019), Svalbard (Sevestre et al., 2015), Canadian Arctic (Blatter and Hutter, 1991; Delcourt et al., 2013) and Chilean Andes (Gacitùa et al., 2015), among the other zones. In any case, it is essential to highlight that the number of scattering events depends not only on the water and/or debris content, but also on the frequency (or, better, on the spectral content) of the antennas used to perform the GPR survey (Björnsson et al., 1996). The theory of electromagnetic scattering from small objects indicates a strong decrease in scattering phenomena from objects much smaller than the wavelengths of the incident wave (Watts and England, 1976), as well as, at the opposite, objects far larger produce distinct reflections rather than diffractions. So, low antenna frequencies can often inhibit the scattering events, preventing the recognition of possible debris and/or water pockets inside the ice volume. In addition, according to Pettersson, 2005, the lack of scattering in low antenna frequency-profiles, compared to the same profiles at high frequency, can be exploited to get an idea on the dimensions of the scatterers.

In order to infer which is the actual meaning of the high scattering facies (HSZ) of the Eastern Gran Zebrù glacier (EGZ) and, more generally, of all the glacier internal features, we adopted a strategy known in medical sciences as "differential diagnosis". In fact, since in many cases there is no direct information (like e.g. core samples) of the HSZ, to limit the subjectivity of interpretation we provide to the readers all the discriminative hypotheses based on both independent and integrated criteria. This is exactly what is done by a physician, which endeavours to organize the objective findings of a patient (as well as some subjective additional complaints!) to decide how to further proceed (Siegenthaler, 2007). In medical sciences, as well as in other fields like in physical models' implementation, this approach is often chosen because a diagnosis in conventional sense is not always achievable and because different possible diagnoses can be done at the same time. There is another important similarity of the approach we choose with the medical differential diagnosis in which for a proper evaluation of the symptoms and risk factors the knowledge of their actual clinical meaning is crucial (Siegenthaler, 2007): in our case, we try to critically evaluate the meaning and consequences of the different factors and analyses, rather than exclusively listing all the different possibilities. With this in mind, in the following sections we analyse our data at first separately and then in an integrated way, critically analysing pros and cons for the different possible interpretations and attributions of the internal structures of the glacier. The working hypothesis is that, in our case study, the scattering facies is not actually related to water content and warm ice, but to an older ice body, masked by the recent EGZ. This former glacial body could be related to a period of negative mass balance in which the glacier underwent a significative shrinking, simultaneous to an enrichment of debris coming from the lateral rocky walls. We combined methodological processes, such as GPR attribute analysis, migration algorithm effects, reflection analysis, and antenna frequency evaluations with geomorphological and remote sensing evidence and correlations to better characterize the EGZ internal facies.

Beside this case study, we guess that this approach could be helpful in many GPR glaciological surveys, in which the target is not only related to the bedrock detection or to the imaging of peculiar glaciological or cryological structures (e.g. crevasses, moulins, permafrost table, …) but also to the thermal regime evaluation. In this perspective, under climate warming conditions, temperate environments with primarily polythermal glaciers could become temperate with both persisting retreat and basal permafrost degradation, as well as cold glaciers can became polythermal or even warm ones in a relatively short time.

2. Study area

The Gran Zebrù glacier (46°28′21"N; 10°34′08″E) is located in Ortles-Cevedale group in the Southern Rhaetian Alps (Central Italian Alps). The glacier is included in the Italian Glacier inventory with ID 502 (Smiraglia and Diolaiuti, 2015). It is a mountain glacier and it is located in Cedec Valley, Valtellina upper Valfurva (SO, Italy). The investigated glacier is the eastern tongue of the glacier lying between about 3000 up to 3250 m asl on a mainly metamorphic bedrock. The glacier accumulation area is bounded by the Pale Rosse peak, the southern slopes of Mt. Gran Zebrù, and Punta Graglia peak (Fig. 1).

The geology of the area is quite complex because different rock types are present, including sedimentary limestones (Calcare di Quattervals), magmatic bodies (Gran Zebrù pluton) and metamorphic rocks. Furthermore, in the area, there is an important tectonic lineament (Gran Zebrù Thrust) that is still seismically active with the last significant event recorded on 20 April 1907 (4.0 Richter scale, Albini et al., 1994) and that presumably constrained the evolution of the through in which the Eastern tongue of the Gran Zebrù glacier is flowing down. The glaciers of the Ortles-Cevedale Group have undergone an impressive shrinkage, approximately 40% from 1954 to 2007 (D'Agata et al., 2014; Smiraglia and Diolaiuti, 2015). Indeed, the Gran Zebrù glacier was a trilobate glacier until 1997 when the easternmost part was completely detached and almost totally covered by debris (Gran Zebrù I, ID 502.1). Since 2010 the easternmost part of the Gran Zebrù glacier is completely melted, and the former central tongue is nowadays called as Eastern Gran Zebrù glacier (EGZ).

The EGZ since 2019 is fully monitored in the frame of the project "Glacier CC" funded by Stelvio National Park with a snow lapse rate cam for the snow and debris accumulation while repeated digital elevation models (DEMs) through a UAV flight monitor the incoming volume and areal changes. Moreover, climate parameters like air temperature, air humidity, wind speed and direction, incoming radiation and ground surface temperature are also monitored at the foot of the glacier front, as well as the melting water flowing of the two main creeks. The mean summer (JJA) air temperature in 2020 was 4.2 °C, while for the hydrological year 2019/2020 the total snow accumulation was averagely 0.2 m of water equivalent and the ice ablation of the frontal part averagely −1.78 m of w.e. with a net balance of ca. -1.58 m of w.e. The mean annual air temperature (MAAT) and mean summer (JJA) air temperature (MSAT) at the mean elevation of the EGZ (i.e. 3170 m a.s.l.) for the period 1997–2020 were equal to −2.1 °C and 4.7 °C, respectively. Considering only the period 2010–2020, the MAAT was equal to −2.2 °C while the MSAT to 5.0 °C. Mean monthly temperatures were extrapolated and annually averaged through the lapse rate obtained with linear regressions (all R2 > 0.75) of the three closest automatic weather stations (AWSs) that shared the longest climatic record: La Vallaccia (46°29′41" N, 10°12′28" E, 2655 m a.s.l.), Valdisotto (46°27′41" N, 10°20′37″ E, 2225 m a.s.l.), Cancano (46°31′61" N, 10°19′14″ E, 1948 m a.s.l.).

The continuous debris cover is mainly concentrated on the eastern side of the glacier occupying about the 15% of the total area with a thickness ranging between 2 and 46 cm, while the rest of the frontal part is characterized by a sparse debris cover (15% of total area), (Tarca and Guglielmin, 2021).

Table 1
List of measurements in 2019 and 2020 with their technical parameters.

|		Survey year			
		2019		2020	
GPR	Number of profiles	33		11	
	Total profiles length [km]	6.1		2.5	
	Central frequency antenna [MHz]	100	250	250	
	Window length [ns]	1034.15	907.18	907.18	
	Sampling interval [ns]	0.50	0.22	0.22	
	Vertical stacking	4		4	
				RGB	Thermal
	Markers	6		17	32
	Mean reprojection error [px]	0.63		0.67	0.36
	Mean markers error [px]	3.5		1.9	0.5
	Orthophoto resolution [cm]	2.8		3.3	11.8
UAV	DEM resolution [cm]	11.2		13.2	/

3. Methods

3.1. Remote sensing

During the study period two photogrammetric UAV surveys have been performed. The first one was done on 17 September 2019 and the second on 17 September 2020. Such data allow to reconstruct the DEM of the glacier and its surrounding and to give a detailed base map for the GPR datasets. For both the photogrammetric surveys, a DJI Matrice 210 Real Time Kinematic (RTK) drone was used with a RTK GPS antenna able to geotag each photogram with a vertical accuracy of 2 cm. The flight missions consisted of a nadir photomosaic acquisition (Carbonneau and Dietrich, 2017) that followed the topography at a constant elevation equal to 130 m above it. Due to a camera upgrade, in 2019 a Zenmuse X5S was used (20.8 MP, focal length 15 mm, micro 4/3 sensor), while in 2020 a Zenmuse XT2 was used (12.0 MP, focal length 8 mm, 1/1.7″ sensor). A total of 659 and 912 photograms were taken in 2019 and 2020, respectively. Images were overlapped for at least 60% both on X and Y axes. The software Agisoft Metashape 1.5 was used to process the two sets of images. The main difference derived from the camera upgrade consisted of a slightly different DEM (11.2 px/cm in 2019, 13.2 px/cm in 2020) and orthophoto resolutions (2.8 px/cm in 2019, 3.3 px/cm in 2020), as well as a reduction of the mean markers' error (3.5 px in 2019, 1.9 px in 2020) (Table 1). The Zenmuse XT2 also acquired thermal infrared (TIR) photograms (640×512 px, focal length 19 mm, 0.1 °C of resolution, 2.0 °C of absolute accuracy), with such a good pair overlap (>80%) that allowed to build a TIR orthomosaic. The thermal parameters were set according to the environmental condition of the surveying day (Shea and Jamieson, 2011), with the emissivity of ice set at 0.97 (Aubry-Wake et al., 2015). TIR processing parameters are shown in Table 1. This was useful for the ice and rock segmentation based on their differences of surface temperatures. Although the temperature accuracy of the camera is only ± 2.0 °C, for many applications precise absolute temperatures are not the most important information,
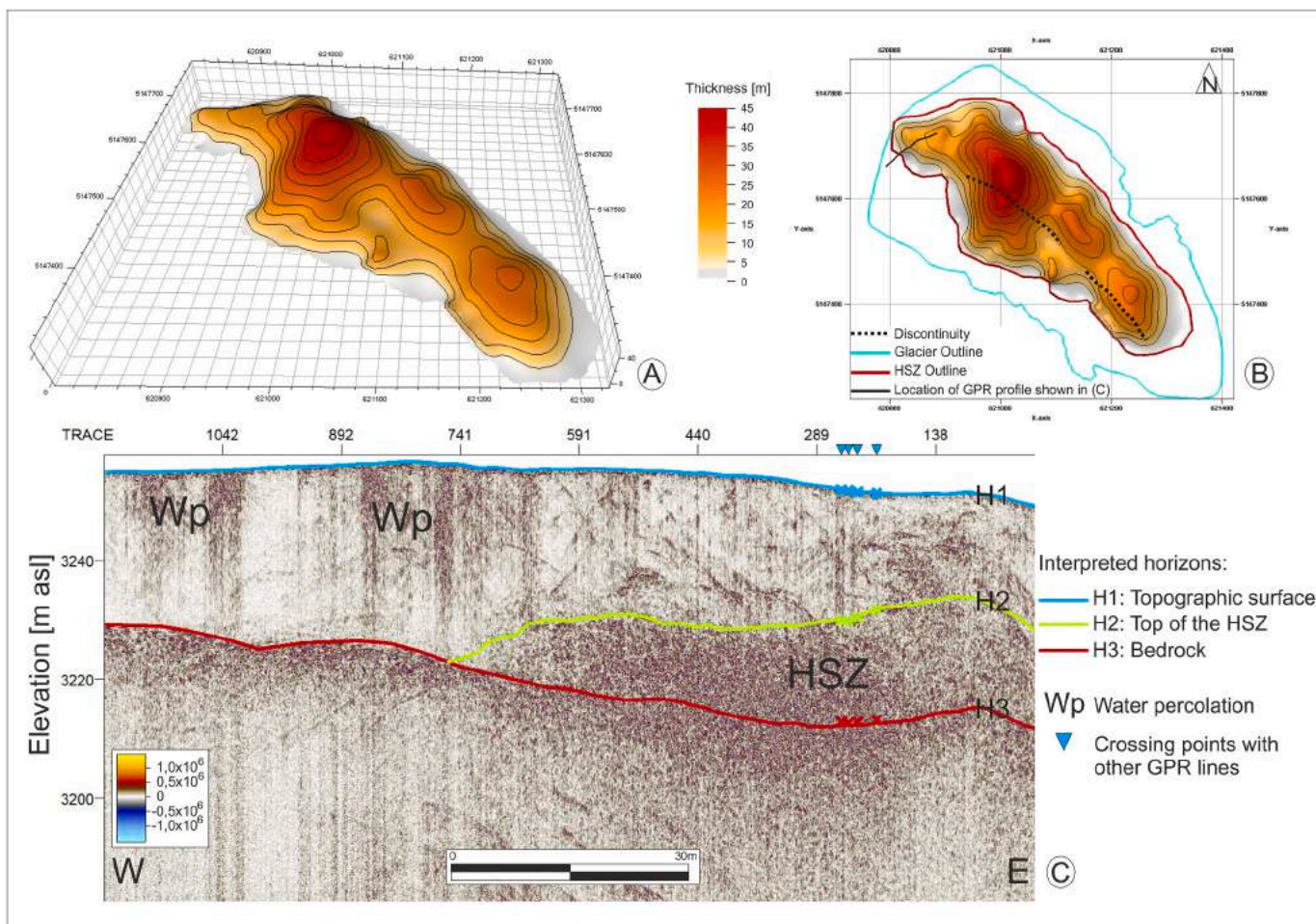
Fig. 2. Area and geometry of the HSZ in 3D (A) and 2D (B) where it is compared with the present glacier border (in light blue). In (C) a GPR section, collected with a 250 MHz antenna during the 2020 survey and containing both transparent and scattering facies, is displayed. Blue triangles on horizontal trace axis and the corresponding crosses on the horizons mark the crossing points with other GPR lines from the same survey. (For interpretation of the references to colour in this figure legend, the reader is referred to the web version of this article.)
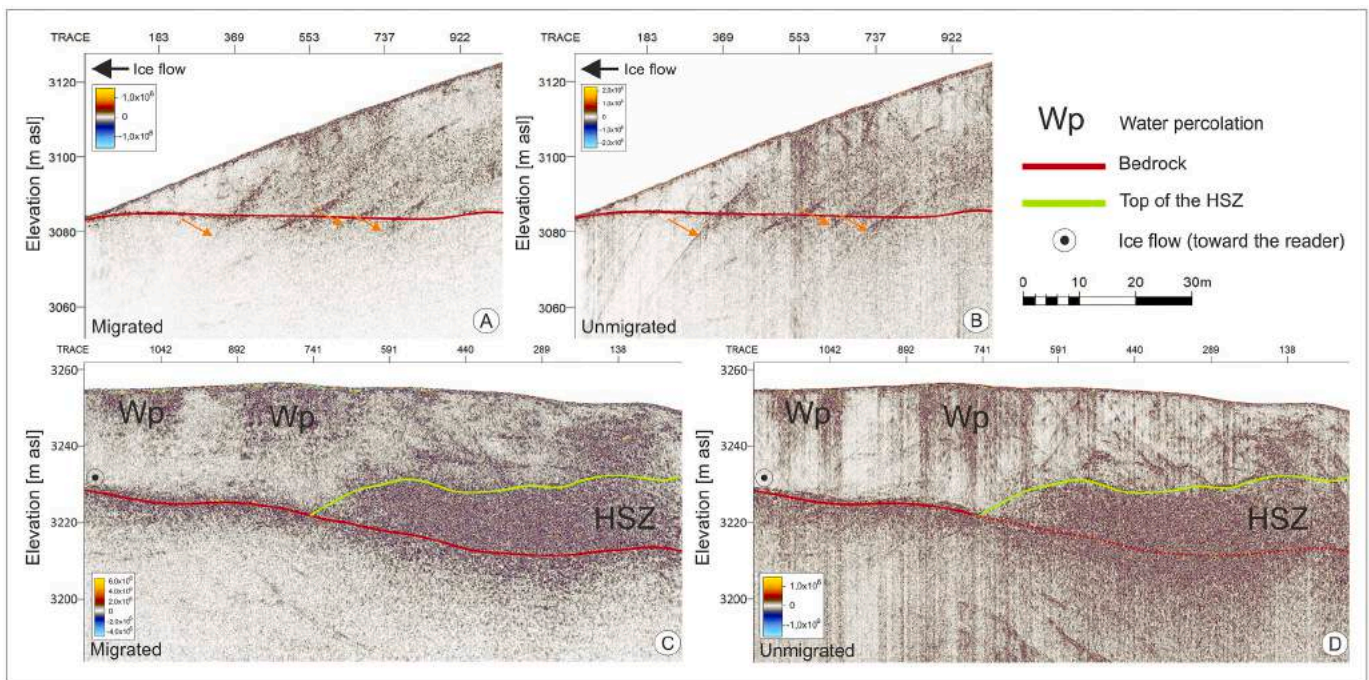
Fig. 3. Comparison of migrated and unmigrated exemplary GPR profiles, located at the front (A) and (B), and at the top (C) and (D) of the EGZ. Orange arrows highlight some effects of migration, correcting the geometrical characteristics of the reflectors/diffractors. WP: water percolation effects.

but gradient maps can reveal unexpected or even unknown thermal patterns (Boesch, 2017). However, in order to increase the camera accuracy, the whole TIR orthomosaic was corrected with the temperature of the water of the southern front glacier stream. The sensor showed an almost constant water temperature of 0.8 °C during the UAV survey.

3.2. Ground Penetrating Radar (GPR)

We performed some ground-coupled GPR surveys on the Eastern Gran Zebrù glacier (EGZ): in detail in August and September 2019 and in September 2020. All the data have been collected with a ProEx (Malå Geoscience) GPR system, equipped with 100 MHz or 250 MHz shielded antennas in the August 2019 survey and with the 250 MHz ones in the other two. The first survey was in fact dedicated to test the performances of the antennas and of the acquisition parameters and, after carefully data analysis, we found that the best results were obtained with 250 MHz antennas, offering the best trade-off between resolution and penetration depth. A total of 6.1 km and of 2.5 km GPR profiles have been collected in 2019 and 2020, respectively (Fig. 1). GPR was triggered by an electro-mechanical odometer allowing a constant trace interval equal to 0.1 m (0.2 m for 100 MHz survey), while a differential GPS device (Magellan Promark II) was used for trace positioning (dm location accuracy). GPR datasets were processed using Prism Software (Radar System Inc.) as well as some in-house module implemented in Matlab. The processing flow includes drift removal (zero-time correction), bandpass filtering (corner frequencies are 20–100–250-600 MHz, with a typical not symmetrical trapezoidal shape to limit Gibbs phenomena), background removal, exponential amplitude recovery, topographic (static) correction, 2D Stolt f-k migration, and depth conversion. The primary purpose of the processing is to increase the signal/noise ratio to improve imaging while maintaining the original data signature, so making the data more easily interpretable and extracting most of the information. The EM velocity used for both depth conversion and migration was set equal to 17 cm ns^{-1}, which is the value typical for pure ice. It is quite obvious that local velocity variations from such a value are surely present, mostly caused by free water, but Common Offset data do not allow to reconstruct an accurate and precise velocity field and nonetheless the checks done on migrated profiles gives quite good and realistic results, with only limited local artifacts. Moreover, we remark that the objective of this paper is to characterize the internal facies of a glacier rather than estimating its thickness. During data interpretation, we focused on the different EM signatures apparent along GPR profiles. We first performed a GPR attribute analysis of processed data to better understand the internal structure of the glacier and to figure out the physical sources of scattering (water/air pockets, debris). GPR attributes are conceptually similar to seismic ones, but although application of GPR attributes can be found in archaeology (Zhao et al., 2016), structural geology (McClymont et al., 2008) and hydrocarbon analogue reservoir imaging (Forte et al., 2012), they are still not routinely applied as a standard procedure for GPR data analysis and interpretation. In glaciology, as far as we know, the only application of attribute analysis is provided by Zhao et al., 2016 and Lu et al., 2020, both proposing strategies to combine different attributes to improve accuracy and validity of GPR interpretation. Another reported use of GPR attributes is for automated reflectors picking (Dossi et al., 2015). Thanks to its, at least theoretical, GPR dependence to the intrinsic attenuation of the EM signal, we exploited especially frequency-related attributes to identify zones with higher losses, which could be further related to higher water content in turn responsible for local higher electrical conductivity. Also, we calculated and imaged the composite attribute of sweetness, which favors the detection and the boundaries between zones having different physical characteristics, often enhancing the signature of the reflection amplitudes. Further analyses focused on: migration effects, comparison of data from different central frequency antennas and polarity assessment.

4. Results and discussion

During the interpretation of the EGZ dataset, we identified different internal units on the basis of geophysically imaged structures and GPR signal characteristics. We easily recognised a layer almost transparent from the EM point of view, which is referred as almost clean ice. Several close diffraction hyperbolas and internal reflections are diagnostic for some glaciological structures such as crevasses visually noticed at the
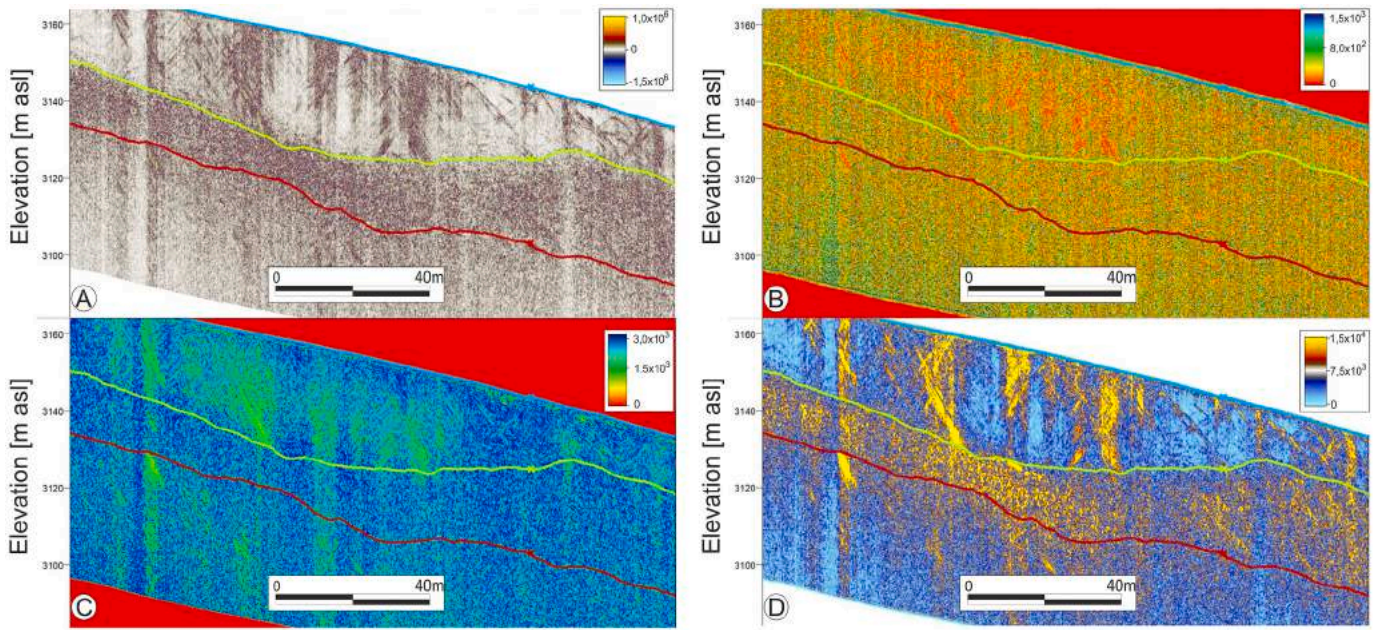
Fig. 4. Exemplary not migrated GPR profile of the EGZ. (A) reflection amplitude (i.e. usual processed data), (B) instantaneous bandwidth, (C) dominant frequency, (D) sweetness. Light-blue, green and red lines mark the horizons of topographic surface, top of scattering facies and bedrock, respectively. (For interpretation of the references to colour in this figure legend, the reader is referred to the web version of this article.)

surface also during the survey. The chosen period for all the acquisitions (early autumn) results in high quantities of surficial flooding water, which also percolates inside the ice through the crevasses, creating disturbing effects noticeable in the shallow portions of the glacier in many surveyed areas (Fig. 2). However, the percolation of water does not strongly affect the amplitude of the ice-rock contact reflection, which is clearly visible with a strong amplitude, below the almost transparent EM facies. The ice-bedrock contact has a totally different signature below a second EM facies, which is characterized by high amplitude scattering (FIG. 2). This high scattering zone (HSZ) has quite abrupt top and lateral limits, while its bottom is more elusive, although the bedrock can be, at least locally, identified.

5. Imaging

5.1. Shape and location of HSZ

We identified the HSZ on the datasets acquired in two consecutive years, i.e. 2019 and 2020. From both of them, we were able to reconstruct the shape of the scattering body, which resulted to be mainly the same, with minor differences mostly due to a denser dataset collected in 2019. The scattering body covers an area of about 111,500 m^2 equal to more than 50% of the whole EGZ area (218,100 m^2) and has an elongated shape, extending downslope from NW to SE (FIG. 2). The mean and maximum thicknesses of the scattering body are equal to about 20 m and 45 m, respectively, while its estimated volume (2,159,000 m^3) represents nearly the 40% of the whole glacier (5,451,000 m^3). Analysing the HSZ distribution (Fig. 2B), we observed that it is localized in a central and well-defined sector of the glacier, corresponding to a longitudinal incision of the bedrock. It is interesting to note that no evidence of scattering facies was found on GPR profiles close to the lateral walls containing the glacier area. There is a sharp lateral transition between the transparent facies of clean ice and the scattering body (FIG. 2) which is unlikely associated with free water. Additionally, on GPR profiles it is evident that surficial water percolates inside the ice, suggesting that some water in the scattering facies comes from surface. Indeed, although water penetrates the ice thickness, we noticed that going down toward the bedrock, the GPR response is often transparent

and evident, as the high amplitude reflection of ice-bedrock contact (Fig. 2C). So, supposing that the water responsible of scattering phenomena had a surficial origin, the scattering facies should have a spatial distribution extremely localized and roughly superimposable with the crevasses position. As described before, the HSZ is located in an extended and well-defined area, which shows no correlation with crevasses position and which is almost identical in two consecutive years, making difficult correlations with water-related phenomena, which typically show relevant seasonal and annual variations. In addition, we measured the slope of the HSZ close to the present front of the EGZ: it shows a sharp lateral transition and a mean dip of almost 40° (Fig. 3). This geometry is difficult to be attributed to a frozen body characterized by free water inside it.

Wp: water percolation effects. Black dotted line highlights a longitudinal discontinuity apparent on photogrammetric data (see section 7 and Fig. 10b for further details).

5.2. Migration analysis

Migration techniques focus on developing more spatially and physically realistic images of the subsurface, by moving from a vertical TWT-scale to a depth-scale, correcting the geometrical properties of reflectors (i.e. adjusting their position, slope and length), and removing the disturbing effects due to diffractions. We decided to apply a Stolt f-k migration algorithm with a 3.1 relative electrical permittivity value corresponding to a constant velocity of 17 cm ns^{-1}, typical of pure ice.

We chose such an algorithm for the low computational resources required and its good results with smoothed velocity fields, or a constant velocity field, as in our case.

The results of migration are displayed in FIG. 3: the sloping reflectors in Fig. 3A and B which happened to extend inside the glacier bedrock in the unmigrated section, actually end on or close to the ice-rock contact after the migration was applied. Also, the surficial layer of transparent ice results much cleaner and free from disturbing effects caused by water percolation, allowing to better define the upper limit of the scattering facies (Fig. 3C and D). Therefore, migration shows that the scattering body is in fact imaged as a chaotic unit, but it is contained in a well-defined area, physically separated from the upper and lower units and
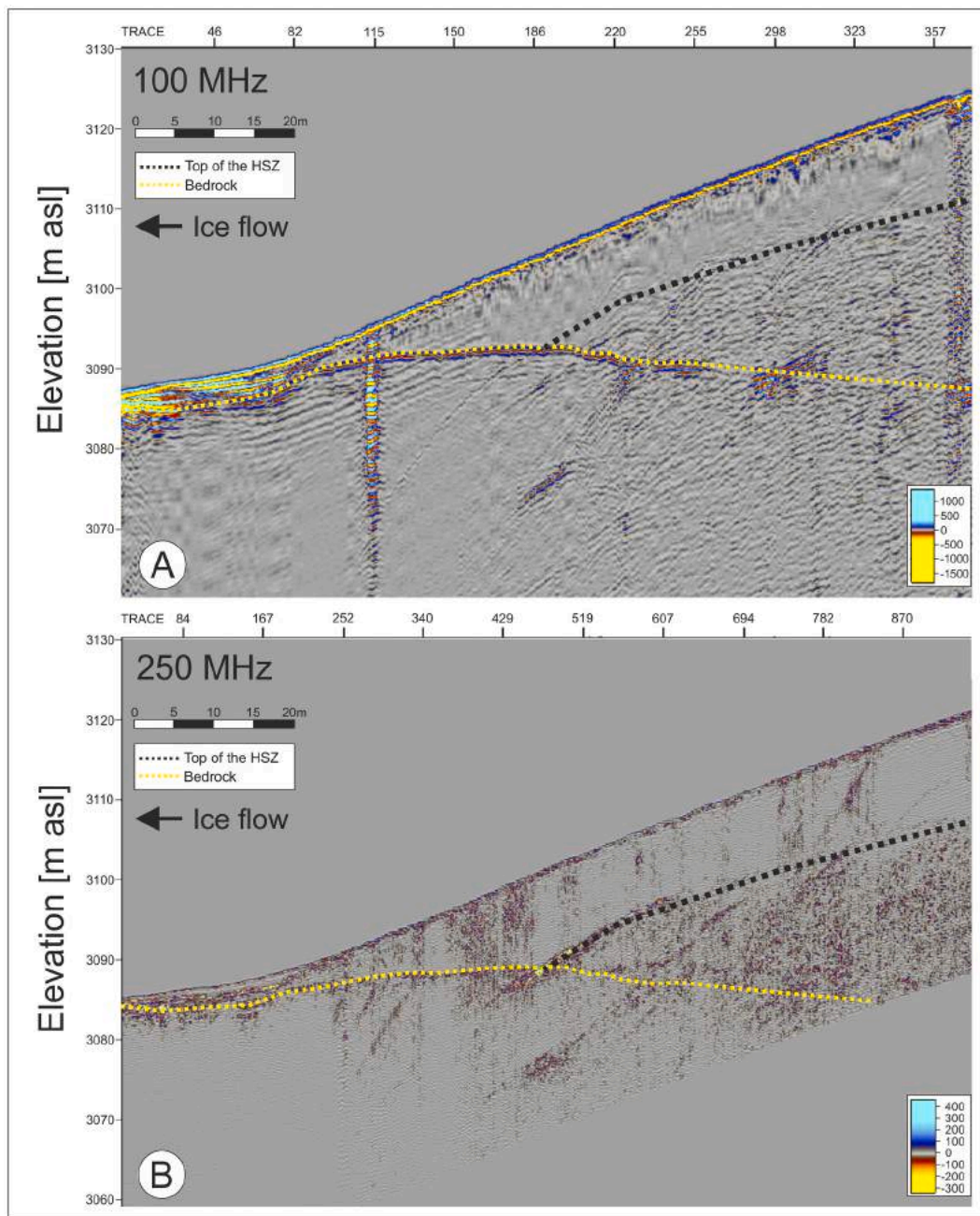
Fig. 5. Comparison between two unmigrated GPR profiles acquired with 100 MHz (A) and 250 MHz (B) central frequency antenna pairs. All the horizons interpreted on 100 MHz profile have been superimposed on 250 MHz one for a better visual comparison. There are some minor discrepancies because the two profiles have been collected a few meters apart.

lying on the glacier bedrock. Moreover, Stolt migration is successful when the lateral velocity gradient is small (or even null). In our case, we observed that the migration was effective because no overmigration artifacts were displayed on the migrated section. So, we can argue that the lateral velocity gradient between the transparent and the scattering unit must be small enough, in turn suggesting that the latter is mainly composed by a material with a EM velocity close to the ice, such as ice and debris. A remarkable free water content would instead produce a high EM velocity decrease since unfrozen water has a 3 cm ns^{-1} EM velocity (West et al., 2007).

6. GPR attribute analysis

We implemented an attribute analysis to support the interpretation

of the EGZ dataset, and, in particular, to better characterize the glaciological EM facies. We exploited the well-stocked database for attribute analysis provided by Petrel Schlumberger interpretation software set and tailored for GPR data. Among several available categories of attributes, we focused on frequency-related ones, due to their high sensitivity to changes of intrinsic attenuation and spectral characteristics of the EM signal. As a matter of fact, high conductivity materials, such as water, strongly affect the attenuation and the frequency spectrum of the EM signal, so we selected "dominant frequency" and "instantaneous bandwidth" attributes, in order to infer the presence of water as responsible for the scattering facies. We also calculated the sweetness attribute, which allows to enhance the boundaries between zones with different physical characteristics, highlighting high amplitude ones. At the opposite, texture attributes, which can be helpful in glaciological
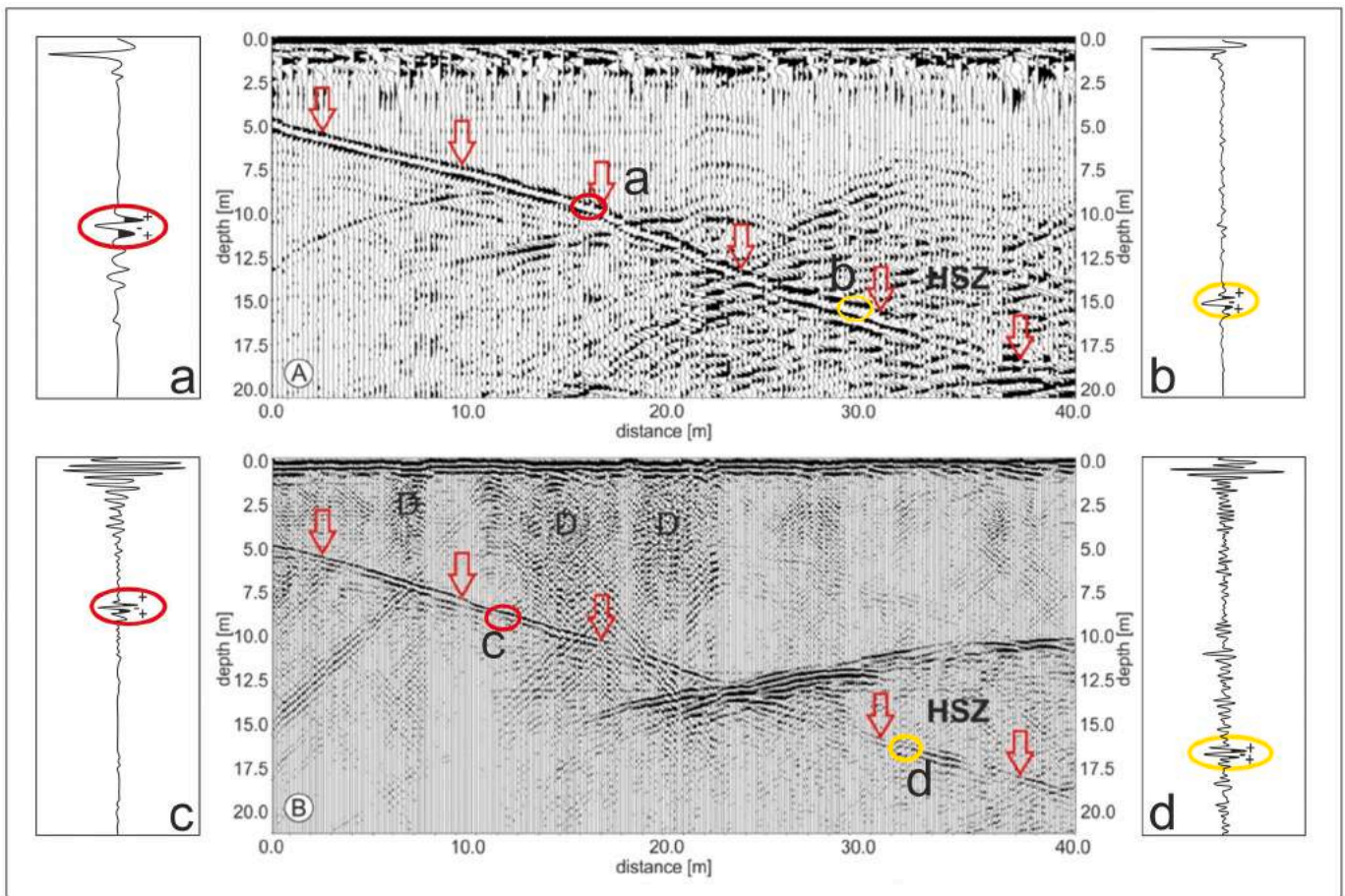
Fig. 6. Portion of 100 MHz (A) and 250 MHz (B) not migrated profiles along the same path, close to the front of the glacier, acquired during the 2020 survey. Red arrows point to the bottom glacier reflector. HSZ and D labels refer to the high scattering zone and to the surficial diffractions, respectively. 250 MHz profile has double trace number as compared with the 100 MHz one. Letters a, b, c, d refer to single traces displayed. See text for further details. (For interpretation of the references to colour in this figure legend, the reader is referred to the web version of this article.)

studies (Zhao et al., 2016; Lu et al., 2020) here did not provide relevant additional information.

As described in Forte et al., 2020, in the presence of diffuse water pockets, the analysis of the dominant frequency should reveal an anomalous decrease of the high frequency components related to the scattering facies. A further decrease of its trend, below the high-scattered area (shadow zone) should be noticed as a result of a stronger low-pass filtering effect due to free water within frozen materials. Moreover, the instantaneous bandwidth should follow the same trend of dominant frequency, shrinking in correspondence of high conductivity materials. Fig. 4A shows the amplitude display of a representative profile acquired on EGZ in 2020. We observed that the first layer is characterized by the almost transparent facies typical of pure ice, although the surface is contaminated by diffuse water, with crevasses easing the downward water percolation with a mechanism of over deepening of water-filled crevasses, or hydrofracturing (Benn et al., 2009). Along the water-filled crevasses, both the GPR frequency and the bandwidth decrease, as expected, reaching the lowest values, as a consequence of the high-frequencies absorption due to the percolating water (Fig. 4B and C). On the contrary, it is evident that the scattering facies has spectral characteristics similar to the transparent facies, except in the zones characterized by water percolating from the surface. As a matter of fact, both the dominant frequency and the bandwidth trends increase going down along the section, reaching the highest values close to the bottom, which is characterized by high-frequencies, related to environmental random noise. Fig. 4D shows the composite sweetness attribute which allows to better highlight the boundaries of each facies. In

the sweetness display, the ice-bedrock contact can be better identified even below the scattering facies, where it is characterized by values of sweetness lower than the area with water percolation. So, considering the increase of both dominant frequency and bandwidth trends, as well as the characteristics of the sweetness, it is unlikely that the scattering facies is related to remarkable quantities of water.

7. Antenna frequency

Fig. 5 shows the comparison of two profiles, spaced a couple of meters from each other and located at the front of the EGZ, acquired with 100 MHz (Fig. 5A) and 250 MHz central frequency antennas (Fig. 5B). The 250 MHz frequency antenna provides more detailed imaging of the glacier internal structures, allowing to better characterize the EM facies and the boundaries among frozen materials, which are barely perceivable, but still recognizable, in the 100 MHz profile.

As already stated in the previous paragraph, the transparent facies is contaminated by water percolation effects visible as sub-vertical scattering, which is evident especially in the 250 MHz profile. Such a scattering is not recognizable in 100 MHz profile, where the shallowest glaciological unit results in an almost totally transparent facies. Instead, the scattering events of the HSZ can still be recognised in the 100 MHz profile, although in smaller amount. According to the scattering theory (e.g. Jol, 2009), for a 250 MHz frequency, only objects with an order of magnitude of around 6×10^{-1} m can produce scattering events. On the contrary, the dimensions of the scatterers increase to around 1.7 m with a 100 MHz frequency. Considering that only the clean ice unit
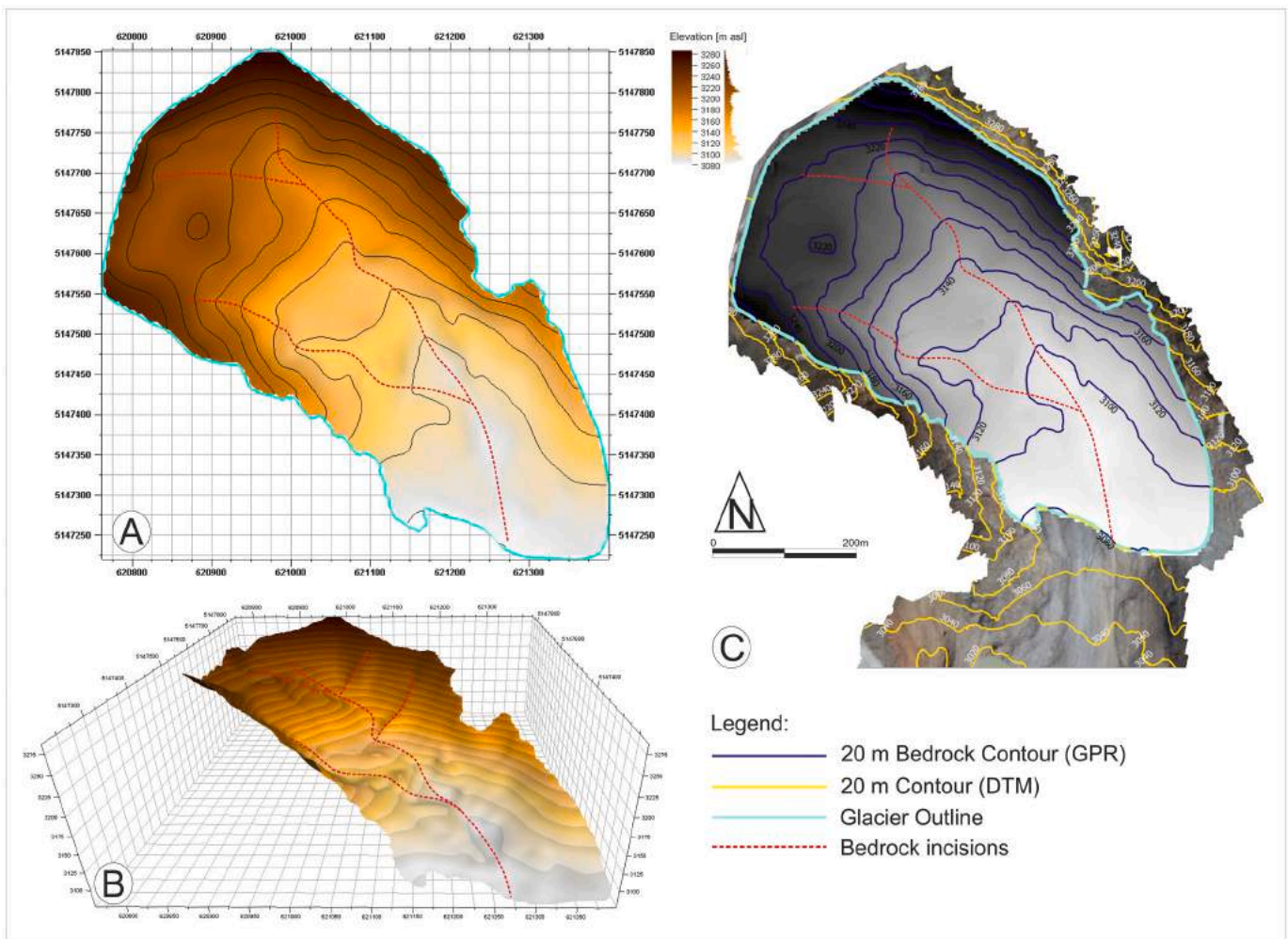
Fig. 7. EGZ bedrock reconstruction. Planar view (A); 3D view (B); mosaicking of contour lines from GPR and DTM data (C).

characterized by water percolation was affected by the decrease of the frequency, while the HSZ shows the scattering phenomena in both profiles, we conclude that the scattering facies below the clean ice should be related to another unit, most likely due to ice containing debris rather than high quantities of free water. The debris may be composed of unclassed sediments containing clasts about $10^{-2}/10^{-1}$ m in size, enough to scatter the EM incident wave at 250 MHz, and also bigger clasts, producing some scattering at 100 MHz central frequency.

8. Reflection amplitude and polarity

Another helpful analysis is the evaluation of reflection amplitudes and polarity. In fact, both parameters give information about the nature of the interfaces and, in turn, on the materials above and below them. Such analysis is a quite common approach for quantitative GPR evaluations and was also applied to define areas with water close to the ice bottom reflection (Pattyn et al., 2009). The reflection coefficient is a measure of the amount of energy reflected at an interface between two different media and depends mainly on the electrical permittivity (a rigorous description is out of the scope of this paper and can be found, for instance, in Ward and Hohmann, 1988). In glaciology, the reflection amplitude analysis takes advantage due to the properties of the involved materials (i.e. ice, free water, rocks, debris and sediments, air) which can produce reflection coefficients spanning from about −0.8 up to about +0.8 (Bælum and Benn, 2011) in turn determining very high-amplitude reflections. Water has a relative dielectric permittivity close to 80 (in the typical frequency interval used for GPR in glaciology),

which is one order of magnitude higher than most of geological materials being such a physical parameter close to 3 for pure ice, equal to 1 for air, and in the range between 5 and 10 for most of dry coarse sediments and rocks (e.g. Davis and Annan, 1989). As a consequence, the presence of water can be highlighted by a remarkable amplitude increase in the reflection between two media when one of them is filled or saturated by unfrozen water. Such kind of analyses are reported by several authors in different locations and environments (Gades et al., 2000; Pattyn et al., 2009; Young et al., 2016), while Forte et al., 2014 inverted the amplitude of reflectors within glaciers to infer the EM velocity and the frozen materials density. Besides the reflection amplitudes, reflection polarities are crucial to determine the sign of the reflection coefficients. For such evaluation, the first phase of each reflection has to be identified and then compared with the first phase of the transmitted wavelet. In detail, equal polarities in the normal incidence case are caused by an impedance increase with depth, while the contrary occurs when opposite polarities are detected. In the analysis of real GPR data, the first phase of a reflection is often difficult to identify because the transmitted wavelet is generally made of several phases, since a single reflection is actually composed by multiple events, each of them with alternating polarities. In fact, dispersion phenomena can modify the shape of the wavelet with time (especially in high loss environments), and the presence of both random and coherent noise (including diffractions) may cause phase distortions (Dossi et al., 2015).

On EGZ data, it was not possible to quantitative analyse (or invert) the reflection's amplitudes due to the high overall scattering and the effects due to the water percolating on and within the glacier. For the
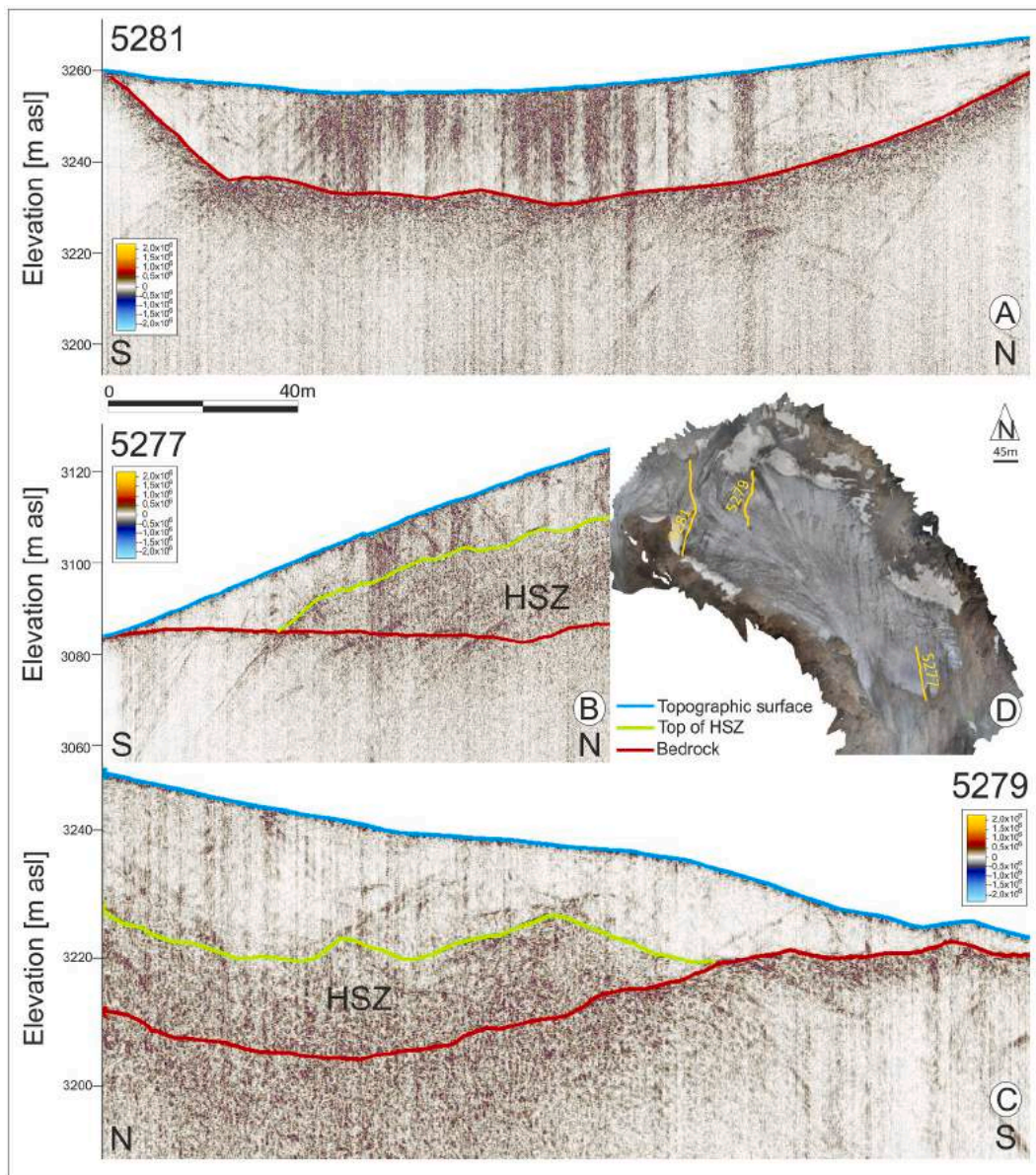
Fig. 8. Three exemplary not migrated GPR profiles of the EGZ showing both the HSZ and the transparent clean ice facies (A, B, C) and the 2020 orthophoto with their location superimposed (yellow lines in D). (For interpretation of the references to colour in this figure legend, the reader is referred to the web version of this article.)

same reasons we did not perform the phase assessment because the actual polarity of the reflector is not always clear. However, we analysed the behaviour of the bottom glacier reflector lying below both the clean ice and the HSZ (Fig. 6). We found that the polarity of such a reflector does not change below the two different facies. If the HSZ would be associated with a higher free water content within warm ice, the reflector at its base should be characterized by a phase inversion with respect to the polarity below the EM transparent ice, but this is never the case. This behaviour is apparent on both 100 and 250 MHz data, while the scattering appearance is very different. In FIG. 6, we highlighted that the bedrock reflection keeps its polarity, characterized by the same phases, below both the EM transparent ice and the HSZ.

9. Bedrock reconstruction

The availability of more than 8.5 km of GPR profiles covering all the glacier extension allowed to reconstruct the morphologies of the bedrock with a good detail level. It extends from 3080 to 3280 m asl, with the slope ranging from 4° to 50°, being the steepest dips related to

the lateral walls limiting the glacier toward North-East and South-West. The bedrock morphology shows two major converging longitudinal incisions, extending along the entire length of the actual glacier area and joining close to the front (Fig. 7). Smaller incisions coming down from the NE wall can be better highlighted in the 3D bedrock visualization (Fig. 7B). The presence of incisions below the ice thickness do not exclude hypothetical water flows within the HSZ. However, in this latter case we would expect much more localized scattering phenomena, in particular along the incisions and not so distributed in a well-defined and wide area. The patterns of the main bedrock incisions seem following the general pattern of the Zebrù thrust and are independent from the crevasses and the surface water flows paths.

10. Comparison of profiles at different elevations and with different thicknesses distribution

We here compare GPR profiles located at different elevations in order to discuss the different internal structures from a thermal and altitudinal point of view. We chose a profile on top, one at the front of the glacier
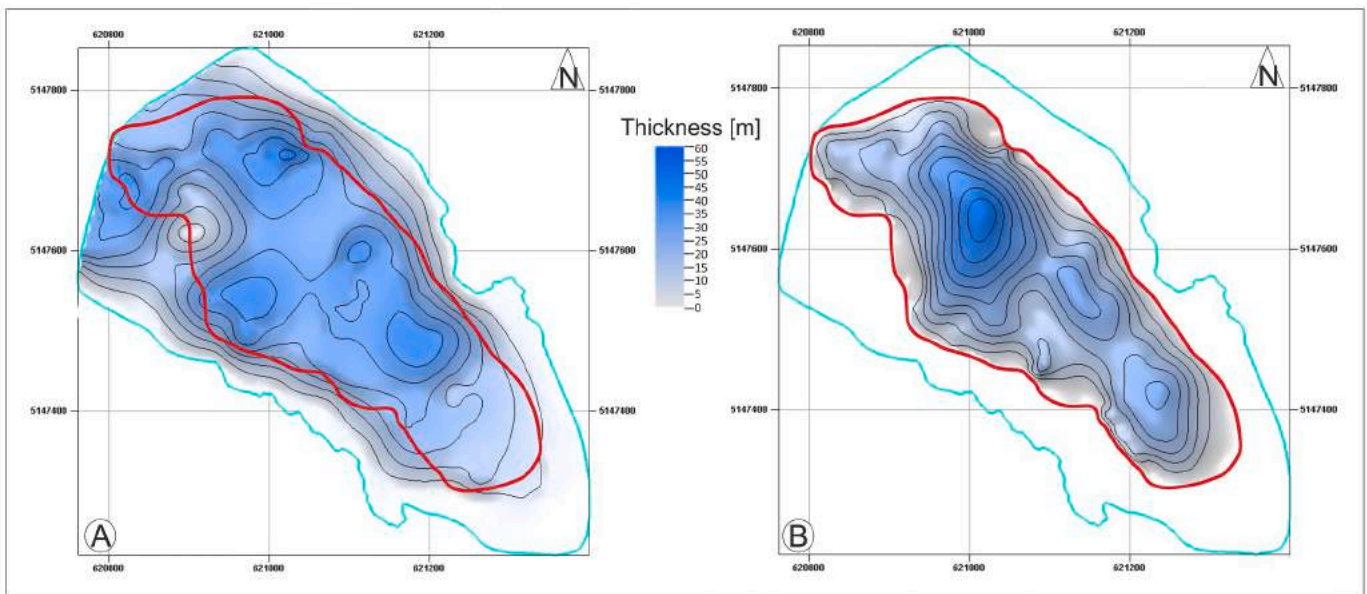
Fig. 9. 2D maps of the clean ice thickness (A) and the HSZ thickness (B), both with the same colour scale for a better visual comparison. Red and light blue lines mark the boundary of the HSZ and of the EGZ, respectively. (For interpretation of the references to colour in this figure legend, the reader is referred to the web version of this article.)

and one with a difference in altitude of about 20 m along it (Fig. 8). In the higher elevation profile (5281), the effect of surficial water percolating inside the ice thickness is quite apparent in the central part of the profile, but except the scattering and the "noising effect", we do not find any evidence of the HSZ in contact with the glacier's bedrock. On the contrary, along profile 5277 (Fig. 8B), it is evident that there is a coexistence of the two facies with a sharp transition between them and, close to the front, the ice is almost transparent from the EM point of view. Moreover, along a profile (5279) with about 20 m difference in altitude (Fig. 8C), the transparent facies extends all along the profile, with higher thickness toward the top. The HSZ instead starts several meters after the beginning of the profile, taking up a deepening of the bedrock and pressing under a progressively thicker ice unit. To complete this analysis, we also considered the distribution of the HSZ in relation with the ice thickness. In Fig. 9 we highlight that the presence of the scattering body is not affected by the ice thickness above it. Supposing a relevant presence of water, it is straightforward to think that the

maximum thickness of scattering is located in correspondence either on the maximum or on the minimum thickness of ice, due to the effect of ice pressure above, or to the external temperature effect, respectively. In our study, no correlation (or anticorrelation) was found between the HSZ and the ice thickness. The lateral gradient of the decrease of clean ice thickness is strictly dominated by the bedrock shape, whose steep flanks limit the extension of the EGZ in particular toward NE and SW. On the contrary, the HSZ outline is not affected by lateral bedrock morphology.

11. Thermography and debris distribution

The thermal mosaic allowed to discriminate the continuous debris cover (17.9%) and rock outcrops (0.7%) that have a temperature always above 0 °C from the glacier ice (81.4%) which is always below or equal to 0 °C, better than a colour classification conducted on the orthophoto. Apart from the continuous frontal sediment, the highest debris
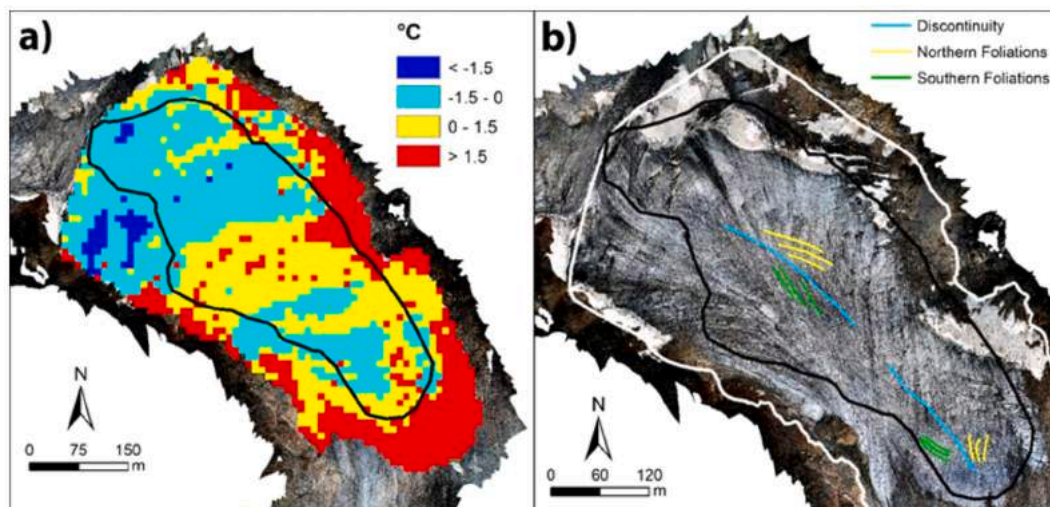
Fig. 10. (a) Thermal orthomosaic classified according to four temperature classes. (b) sharpened orthophoto with a main discontinuity and different foliation angles highlighted. The black line represents the HSZ boundaries as detected by GPR data analysis.

Table 2

Summary of the performed GPR data analysis, the considered parameters, and the resulting characterization of HSZ.

Data analysis	Parameters	Consideration about HSZ interpretation
Imaging Shape and location	Geometrical characteristics of the scattering body	Scattering is contained in a well-defined area with locally sharp lateral transition
Migration analysis	Migrated reflections and diffractions	Successful migration results from low lateral gradient velocity
Attribute analysis	Frequency-related attributes	No low frequency shadow and decrease of bandwidth corresponding at and below the HSZ
Antenna frequency	Amplitude display of 100 MHz and 250 MHz antenna frequency	Surficial scattering due to percolating water exhibits a different signature as compared to the HSZ, especially for lower antenna frequency
Reflection amplitude and polarity	Polarity of ice-bedrock interface	No phase inversion of ice-bedrock interface below the HSZ
Bedrock reconstruction	3D reconstruction from GPR data and DTM	HSZ is not correlated with the bedrock morphology
HSZ location and distribution Elevation	Distribution of facies in relation with elevation	Coexistence of transparent and scattering facies at different elevation
HSZ vs ice thickness	2D distribution of ice vs HSZ thickness	No correlation (or anticorrelation) between HSZ and ice thickness
Thermography and debris distribution	Temperature distribution and spatial analysis of the photogrammetry	HSZ possibly affects the glacier flow along a longitudinal discontinuity, resulting in different foliation angles

concentration was found at the NE side of the glacier. Although the emissivity of glacier ice and rocks had been kept constant at 0.97 and this usually yields low surface temperature errors (Heinl et al., 2012), after the temperature calibration we obtained glacier ice temperatures ranging from −2.8 to 0 °C. It is true that, in case of low texture areas, a vignetting error was registered (Aragon et al., 2020) and absolute glacier surface temperatures were deviated, however the differences between ice and debris were larger than what found for the ice. Therefore, the 10 m per pixel resampling of the glacier surface allowed to distinguish four classes of surface temperatures, namely: below −1.5 °C, from −1.5 to 0 °C, from 0 to 1.5 °C, and above 1.5 °C. It is apparent that the colder ice lies at the top (W) part of the glacier, with warmer ice at lower elevation and also present at the front. Temperatures in the range of 0–1.5 °C can be associated to ice with discontinuous detritus, which is located in the central and frontal part (Fig. 10). The frequency of the four classes is 2.5% for the lowest temperature attributable to colder ice, 39.2% for the warmer ice, 33.1% for the ice with discontinuous debris and 25.2% for debris.

A sharpening filter applied to the orthophoto highlighted a longitudinal discontinuity zone that divided the northern to the southern part of EGZ. Despite the presence of several crevasses, it is possible to observe the different glacier foliation angles above and below this discontinuity (Fig. 10). Such a behaviour can be related to the presence of the HSZ, which influences the glacier flow, splitting it in two separated portions. This can be surely emphasized by the bedrock morphology (FIG. 7), but the presence of debris in the HSZ has certainly a role. In fact, the

discontinuity follows almost perfectly the HSZ axis (FIG. 2). On the contrary, if the HSZ would be interpreted as warm ice with free water inside, it would have a totally different effect, homogeneously increasing the glacier flux velocity in its central part.

12. Conclusion

GPR data collected on EGZ imaged an HSZ below an EM transparent facies both in 2019 and 2020 surveys. To infer the actual meaning of such a unit, we performed a differential diagnosis based on the integrated analyses of geophysical data, remote sensing measurements and geomorphological evidence. Table 2 summarizes the results obtained by evaluating different data characteristics, processing and considerations, which whole seem to associate the HSZ with a mixture of ice and debris rather than to free water within a warm ice unit. In particular, we analysed: the location and shape of the HSZ which remained almost identical for two consecutive years; processing parameters and physical characteristics (GPR attributes, reflection amplitude and polarity behaviour); geomorphological and glaciological factors; remote sensing data obtained by UAV photo camera and thermal sensors.

The debris enriched ice unit could represent an older degraded glacial body, now masked by the actual EGZ. The lack of ice drilling prevents the direct characterization of the internal structures of the EGZ; however, analysis of samples from cores could support or counter the hypothesis of a debris body, but we would highlight the fact that a core provides only spatially punctual information, which could not fully be representative of units and structures on a large area.

Beside this case study, this approach could be helpful in other GPR glaciological surveys, in which the target is related not only to the bedrock detection, but also to a detailed analysis and geophysical characterization of the internal facies of a glacier. In this perspective, under climate warming conditions, temperate environments with primarily polythermal glaciers could become temperate with both persisting retreat and basal permafrost degradation, as well as cold glaciers can become polythermal or even warm ones in a relatively short time, and accurate and effective monitoring strategies must be developed.

Authors contribution

MG and EF conceived the research. IS and EF wrote the manuscript with the contribution of all the other authors. All the authors contributed to data collection; EF, PG and IS processed and interpreted the GPR dataset, while SP collected the UAV data. MG and RRC provided glaciological analyses. The figures have been prepared by IS, PG, SP and EF. All the authors participated in the discussion and revision of the final version of the manuscript.

Declaration of Competing Interest

The authors declare that they have no known competing financial interests or personal relationships that could have appeared to influence the work reported in this paper.

The authors declare the following financial interests/personal relationships which may be considered as potential competing interests.

Acknowledgments

References

Albini, P., Morelli, G., Stucchi, M., 1994. Alcuni terremoti importanti per l'Alta Valtellina. In: "Studi sismici in Alta Valtellina". I quaderni dell'ISMES 336, 19–42 (in Italian).

Anderson, M.P., 2005. Heat as a groundwater tracer. Ground Water 43, 951–968.

Aragon, B., Johansen, K., Parkes, S., Malbeteau, Y., Al-Mashharawi, S., Al-Amoudi, T., McCabe, M.F., 2020. A calibration procedure for field and UAV-based uncooled thermal infrared instruments. Sensors 20 (11), 3316.

Aubry-Wake, C., Baraer, M., McKenzie, J.M., Mark, B.G., Wigmore, O., Hellström, R.Å., Somers, L., 2015. Measuring glacier surface temperatures with ground-based thermal infrared imaging. Geophys. Res. Lett. 42 (20), 8489–8497.

Bælum, K., Benn, D.I., 2011. Thermal structure and drainage system of a small valley glacier (Tellbreen, Svalbard), investigated by ground penetrating radar. Cryosphere 5, 139–149. https://doi.org/10.5194/tc-5-139-2011.

Barzycka, B., Grabiec, M., Błaszczyk, M., Ignatiuk, D., Laska, M., Ove Hagen, J., Jania, J., 2020. Changes of glacier facies on Hornsund glaciers (Svalbard) during the decade 2007–2017. Remote Sens. Environ. 251, 112060. https://doi.org/10.1016/j.rse.2020.112060.

Benn, D.I., Gulley, J., Luckman, A., Adamek, A., Glowacki, P., 2009. Englacial drainage systems formed by hydrologically driven crevasse propagation. J. Glaciol. 55 (191), 513–523.

Björnsson, H., Gjessing, Y., Hamran, S., Olav Liestøl, J.O.H., Pálsson, F., Erlingsson, B., 1996. The thermal regime of sub-polar glaciers mapped by multi-frequency radio-echo sounding. J. Glaciol. 42 (140), 23–32.

Blatter, H., Hutter, K., 1991. Polythermal conditions in arctic glaciers. J. Glaciol. 37 (126), 261–269. https://doi.org/10.3189/S0022143000007279.

Boesch, R., 2017. Thermal remote sensing with UAV-based workflows. The International Archives of Photogrammetry, Remote Sensing and Spatial Information Sciences 42, 41.

Booth, A., Mercer, A., Clark, R., Murray, T., Jansson, P., Axtell, C., 2013. A comparison of seismic and radar methods to establish the thickness and density of glacier snow cover. Ann. Glaciol. 54 (64), 73–82. https://doi.org/10.3189/2013AoG64A044.

Campbell, S., Affleck, R.T., Sinclair, S., 2018. Ground-penetrating radar studies of permafrost, periglacial, and near-surface geology at McMurdo Station, Antarctica. Cold Reg. Sci. Technol. 148, 38–49. https://doi.org/10.1016/j.coldregions.2017.12.008.

Carbonneau, P.E., Dietrich, J.T., 2017. Cost-effective non-metric photogrammetry from consumer-grade sUAS: implications for direct georeferencing of structure from motion photogrammetry. Earth Surf. Process. Landf. 42 (3), 473–486.

Catapano, I., Gennarelli, G., Ludeno, G., Noviello, C., Esposito, G., Soldovieri, F., 2021. Contactless Ground Penetrating Radar. State of the Art, Challenges, and Microwave Tomography-Based Data Processing. IEEE Geoscience and Remote Sensing Magazine, Imaging. https://doi.org/10.1109/MGRS.2021.3082170.

Church, G., Bauder, A., Grab, M., Rabenstein, L., Singh, S., Maurer, H., 2019. Detecting and characterising an englacial conduit network within a temperate Swiss glacier using active seismic, ground penetrating radar and borehole analysis. Ann. Glaciol. 60 (79), 193–205. https://doi.org/10.1017/aog.2019.19.

Colomina, I., Molina, P., 2014. Unmanned aerial systems for photogrammetry and remote sensing: a review. ISPRS J. Photogramm. Remote Sens. 92, 79–97.

Colucci, R.R., Forte, E., Boccali, C., Dossi, M., Lanza, L., Pipan, M., Guglielmin, M., 2015. Evaluation of internal structure, volume and mass balance of glacial bodies by integrated LiDAR and GPR surveys: the case study of Canin eastern Glacieret (Julian Alps, Italy). Surv. Geophys. 36 (2), 231–252. https://doi.org/10.1007/s10712-014-9311-1.

Colucci, R.R., Fontana, D., Forte, E., Potleca, M., Guglielmin, M., 2016. Response of ice caves to weather extremes in the Southeastern Alps, Europe. Geomorphology 261, 1–11. https://doi.org/10.1016/j.geomorph.2016.02.017.

D'Agata, C., Bocchiola, D., Maragno, D., Smiraglia, C., Diolaiuti, G.A., 2014. Glacier shrinkage driven by climate change during half a century (1954-2007) in the Ortles-Cevedale group (Stelvio National Park, Lombardy, Italian Alps). Theor. Appl. Climatol. 116, 169–190.

Davis, J.L., Annan, A.P., 1989. Ground-penetrating radar for high-resolution mapping of soil and rock stratigraphy. Geophys. Prospect. 37, 531–551.

Del Gobbo, C., Colucci, R.R., Forte, E., Triglav Cekada, M., Zorn, M., 2016. The Triglav glacier (south-eastern Alps, Slovenia): volume estimation, internal characterization and 2000-2013 temporal evolution by means of GPR measurements. Pure Appl. Geophys. 173, 2753–2766.

Del Longo, M., Finzi, E., Galgaro, A., Godio, A., Luchetta, A., Pellegrini, G.B., Zambrano, R., 2001. Responses of the Val d'Arcia small dolomitic glacier (mount Pelmo, eastern Alps) to recent climatic changes. Geomorphological and geophysical study. Geografia Fisica e Dinamica Quaternaria 24, 43–55.

Delcourt, C., Van Liefferinge, B., Nolan, M., Pattyn, F., 2013. The climate memory of an Arctic polythermal glacier. J. Glaciol. 59 (218), 1084–1092. https://doi.org/10.3189/2013JoG12J109.

Dossi, M., Forte, E., Pipan, M., 2015. Automated reflection picking and polarity assessment through attribute analysis: theory and application to synthetic and real GPR data. Geophysics 80 (5), H23–H35. https://doi.org/10.1190/geo2015-0098.1.

Dossi, M., Forte, E., Pipan, M., Colucci, R.R., 2018. Quantitative 3-D GPR Analysis to Estimate the Total Volume and Water Content of a Glacier, 17th International Conference on Ground Penetrating Radar (GPR). Rapperswil, Switzerland, pp. 1–6. https://doi.org/10.1109/ICGPR.2018.8441636.

Eisen, O., Bauder, A., Lüthi, M., Riesen, P., Funk, M., 2009. Deducing the thermal structure in the tongue of Gornergletscher, Switzerland, from radar surveys and borehole measurements. Ann. Glaciol. 50 (51), 63–70.

Forte, E., Pipan, M., Casabianca, D., Di Cuia, R., Riva, A., 2012. Imaging and characterization of a carbonate hydrocarbon reservoir analogue using GPR attributes. J. Appl. Geophys. 81, 76–87. https://doi.org/10.1016/j.jappgeo.2011.09.009.

Forte, E., Dossi, M., Pipan, M., Colucci, R.R., 2014. Velocity analysis from common offset GPR data inversion: theory and application to synthetic and real data. Geophys. J. Int. 197 (3), 1471–1483. https://doi.org/10.1093/gji/ggu103.

Forte, E., Pipan, M., Francese, R., Godio, A., 2015. An overview of GPR investigation in the Italian Alps. First Break 33, 61–67.

Forte, E., Santin, I., Colucci, R.R., Dossi, M., Guglielmin, M., Pipan, M., Roncoroni, G., Žebre, M., 2020. GPR data analysis for cold and warm ice detection and characterization in polythermal glaciers. In: 18th International Conference on Ground Penetrating Radar, Golden, Colorado, 14–19 June 2020. November, 2020, pp. 69–72. https://doi.org/10.1190/gpr2020-019.1.

Fowler, A., Murray, T., Ng, F., 2001. Thermally controlled glacier surging. J. Glaciol. 47 (159), 527–538. https://doi.org/10.3189/172756501781831792.

Fugazza, D., Scaioni, M., Corti, M., D'Agata, C., Azzoni, R.S., Cernuschi, M., Smiraglia, C., Diolaiuti, G.A., 2018. Combination of UAV and terrestrial photogrammetry to assess rapid glacier evolution and map glacier hazards. Nat. Hazards Earth Syst. Sci. 18, 1055–1071. https://doi.org/10.5194/nhess-18-1055-2018.

Gacitùa, G., Uribe, J.A., Wilson, R., Loriaux, T., Hernàndez, J., Rivera, A., 2015. 50MHz helicopter-borne radar data for determination of glacier thermal regime in the central Chilean Andes. Ann. Glaciol. 56, 193–201.

Gades, A.M., Raymond, C.F., Conway, H., Jacobel, R.W., 2000. Bed properties of Siple dome and adjacent ice streams, West Antarctica, inferred from radio-echo sounding measurements. J. Glaciol. 46 (152), 88–94.

Godio, A., 2008. Performance and experimental evidence of GPR in density estimates of snowpack. Boll. Geofis. Teor. Appl. 49, 279–298.

Gusmeroli, A., Jansson, P., Pettersson, R., Murray, T., 2012. Twenty years of cold surface layer thinning at Storglaciären, sub-Arctic Sweden, 1989-2009. J. Glaciol. 58, 3–10.

Hausmann, H., Behm, M., 2011. Imaging the structure of cave ice by ground penetrating radar. Cryosphere 5, 329–340.

Heinl, M., Leitinger, G., Tappeiner, U., 2012. Diurnal surface temperature regimes in mountain environments. Phys. Geogr. 33 (4), 344–359.

Irvine-Fynn, T.D.L., Hodson, A.J., Moorman, B.J., Vatne, G., Hubbards, A.L., 2011. Polythermal glacier hydrology: a review. Rev. Geophys. 49, 4.

Jol, H.M., 2009. Ground Penetrating Radar Theory and Application. Elsevier Science, First Edition.

Karpilo Jr., R.D., 2009. Glacier monitoring techniques. In: Young, R., Norby, L. (Eds.), Geological Monitoring: Boulder. Colorado, Geological Society of America, pp. 141–162. https://doi.org/10.1130/2009.monitoring(06).

Kaser, G., Fountain, A.G., Jansson, P., 2003. A Manual for Monitoring the Mass Balance of Mountain Glaciers with Particular Attention to Low Latitude Characteristics. A contribution to the UNESCO HKH-Friend programme, Paris (France).

King, E.C., Smith, A.M., Murray, T., Stuart, G.W., 2008. Glacier-bed characteristics of Midtre Lovénbreen, Svalbard, from high-resolution seismic and radar surveying. J. Glaciol. 54 (184), 145–156.

Li, J., Paden, J., Leuschen, C., Rodriguez-Morales, F., Hale, R.D., Arnold, E.J., Crowe, R., Gomez-Garcia, D., Gogineni, P., 2013. High-altitude radar measurements of ice thickness over the Antarctic and Greenland ice sheets as a part of operation icebridge. IEEE Trans. Geosci. Remote Sens. 51 (2), 742–754. https://doi.org/10.1109/TGRS.2012.2203822.

Lu, G., Zhao, W., Forte, E., Tian, G., Li, Y., Pipan, M., 2020. Multi-frequency and multi-attribute GPR data fusion based on 2-D wavelet transform. Measurement 166, 108243. https://doi.org/10.1016/j.measurement.2020.108243.

McClymont, A.F., Green, A.G., Streich, R., Horstmeyer, H., Tronicke, J., Nobes, D.C., Pettinga, J., Campbell, J., Langridge, R., 2008. Visualization of active faults using geometric attributes of 3D GPR data: an example from the alpine fault zone. New Zealand. Geophys. 7 (2), B11–B23.

Merz, K., Maurer, H., Rabenstein, L., Buchli, T., Springman, S.M., Zweifel, M., 2014. Multidisciplinary geophysical investigations over an alpine rock glacier. Geophysics 81, WA147–WA157. https://doi.org/10.1190/geo2015-0157.1.

Moorman, B.J., Michel, F.A., 2000. The application of ground-penetrating radar to the study of glacial hydrology. Hydrol. Process. 14, 2645–2667.

Navarro, F.J., Martín-Español, A., Lapazaran, J.J., Grabiec, M., Otero, J., Vasilenko, E.V., Puczko, D., 2014. Ice volume estimates from ground-penetrating radar surveys, wedel Jarlsberg land glaciers, Svalbard. Arctic. Antarctic and Alpine Research 46 (2), 394–406. https://doi.org/10.1657/1938-4246-46.2.394.

Paterson, W.S.B., 1994. Ice Core studies. In: Paterson, W.S.B, the physics of glaciers (third edition). Pergamon 1994, 378–409. ISBN 9780080379449. https://doi.org/10.1016/B978-0-08-037944-9.50021-2.

Pattyn, F., Delcourt, C., Samyn, D., de Smedt, B., Nolan, M., 2009. Bed properties and hydrological conditions underneath McCall glacier, Alaska, USA. Ann. Glaciol. 50, 80–84.

Pellikka, P., Gareth Rees, W., 2010. Remote sensing of glaciers. Techniques for topographic, spatial and thematic mapping of glaciers. 1st edition, CRC Press, Taylor&Francis Group, London, UK, ISBN 9780415401661.

Pettersson, R., 2005. Frequency dependence of scattering from the cold-temperate transition surface in a polythermal glacier. Radio Sci. 40, RS3007.

Pettersson, R., Jansson, P., Holmlund, P., 2003. Cold surface layer thinning on Storglaciären, Sweden, observed by repeated ground penetrating radar surveys. J. Geophys. Res. 108 (F1), 6004. https://doi.org/10.1029/2003JF000024.

Reinardy, B.T.I., Booth, A.D., Hughes, A.L.C., Boston, C.M., Åkesson, H., Bakke, J., Nesje, A., Giesen, R.H., Pearce, D.M., 2019. Pervasive cold ice within a temperate

glacier – implications for glacier thermal regimes, sediment transport and foreland geomorphology. Cryosphere 13, 827–843. https://doi.org/10.5194/tc-13-827-2019.

Rutishauser, A., Maurer, H., Bauder, A., 2016. Helicopter-borne ground-penetrating radar investigations on temperate alpine glaciers: a comparison of different systems and their abilities for bedrock mapping. Geophysics 81, WA119–WA129.

Santin, I., Colucci, R.R., Žebre, M., Pavan, M., Cagnati, A., Forte, E., 2019. Recent evolution of Marmolada glacier (Dolomites, Italy) by means of ground and airborne GPR surveys. Remote Sens. Environ. 235 https://doi.org/10.1016/j.rse.2019.111442.

Sevestre, H., Benn, D.I., Hulton, N.R.J., Bælum, K., 2015. Thermal structure of Svalbard glaciers and implications for thermal switch models of glacier surging. J. Geophys. Res. Earth Surf. 120, 2220–2236. https://doi.org/10.1002/2015JF003517.

Shea, C., Jamieson, B., 2011. Some fundamentals of handheld snow surface thermography. Cryosphere 5 (1), 55–66. https://doi.org/10.5194/tc-5-55-2011.

Siegenthaler, W. (Ed.), 2007. Differential Diagnosis in Internal Medicine: From Symptom to Diagnosis. Thieme publishing group, 1144p., ISBN 9783131421418.

Smiraglia, C., Diolaiuti, G., 2015. Il Nuovo Catasto dei Ghiacciai Italiani. Comitato Ev-K2-CNR ed., Bergamo, 400pp. (in Italian).

Tarca, G., Guglielmin, M., 2021. Using ground-based thermography to analyse surface temperature distribution and estimate debris thickness on Gran Zebrù glacier (Ortles-Cevedale, Italy), EGU General Assembly 2021. online, 19–30 Apr 2021, EGU21–3497. https://doi.org/10.5194/egusphere-egu21-3497.

Thompson, S.S., Cook, S., Kulessa, B., Winberry, J.P., Fraser, A.D., Galton-Fenzi, B.K., 2020. Comparing satellite and helicopter-based methods for observing crevasses, application in East Antarctica. Cold Reg. Sci. Technol. 178, 103128. https://doi.org/10.1016/j.coldregions.2020.103128.

Van der Sluijs, J., Kokelj, S.V., Fraser, R.H., Tunnicliffe, J., Lacelle, D., 2018. Permafrost terrain dynamics and infrastructure impacts revealed by UAV photogrammetry and thermal imaging. Remote Sens. 10, 1734. https://doi.org/10.3390/rs10111734.

Ward, S.H., Hohmann, G.W., 1988. Electromagnetic Theory for Geophysical Applications. Investigations in Geophysics, SEG, Tulsa, 531p.,ISBN 978-0-931830-51-8.

Watts, R.D., England, A.W., 1976. Radio-echo sounding of temperate glaciers: ice properties and sounder design criteria. J. Glaciol. 17 (75), 39–48.

West, J.L., Rippin, D.M., Murray, T., Mader, H.M., Hubbard, B., 2007. Dielectric permittivity measurements on ice cores: implications for interpretation of radar to yield glacial unfrozen water content. J. Environ. Eng. Geophys. 12 (1), 37–45.

Young, D.A., Schroeder, D.M., Blankenship, D.D., Kempf, Scott D., Quartini, E., 2016. The distribution of basal water between Antarctic subglacial lakes from radar sounding. Philosophical Transaction Royal Society, A 374, 1–21. https://doi.org/10.1098/rsta.2014.0297, 20140297.

Žebre, M., Colucci, R.R., Giorgi, F., Glasser, N.F., Raccviteanu, A.E., Del Gobbo, C., 2020. 200 years of equilibrium-line altitude variability across the European Alps (1901−2100). Clim. Dyn. 56, 1183–1201. https://doi.org/10.1007/s00382-020-05525-7.

Zhao, W., Forte, E., Colucci, R.R., Pipan, M., 2016. High-resolution glacier imaging and characterization by means of GPR attribute analysis. Geophys. J. Int. 206, 1366–1374. https://doi.org/10.1093/gji/ggw208.